MOX–Report No. 10/2007

Modelling and Numerical Simulation for Yacht Engineering

Nicola Parolini, Alfio Quarteroni

MOX, Dipartimento di Matematica "F. Brioschi"
Politecnico di Milano, Via Bonardi 29 - 20133 Milano (Italy)

mox@mate.polimi.it http://mox.polimi.it

Modelling and Numerical Simulation for Yacht Engineering

N. Parolini[(1)], A. Quarteroni[(1,2)]

31st May 2007

[(1)] CMCS - Institut d'Analyse et Calcul Scientifique
Ecole Polytechnique Fédérale de Lausanne
Station 8, CH-1015, Lausanne, Switzerland

[(2)] MOX– Modellistica e Calcolo Scientifico
Dipartimento di Matematica "F. Brioschi"
Politecnico di Milano
via Bonardi 9, 20133 Milano, Italy

Abstract

In the past few years, Computational Fluid Dynamics (CFD) has become an essential tool in the design and optimization of racing sailboats and in particular America's Cup yachts. The prevalent role of CFD in the design process is demonstrated by the number of numerical simulations on different boat features, ranging from hull and appendage design to sail optimization, that each America's Cup syndicate carries on during the boat design and its further development.

In this work, we report some of the numerical results obtained in the framework of the research partnership between the Ecole Polytechnique Fédérale de Lausanne (EPFL) and the Alinghi Team, in preparation to the 32$^{\text{nd}}$ edition of the America's Cup. A particular attention is devoted to the innovative aspects of the numerical models that have been recently developed.

Introduction

An America's Cup yacht is a very sophisticated system that should operate optimally in a wide range of sailing conditions. The different components (above and beneath the water surface) of a sailing yacht interact one another through several complex relations. The design of an America's Cup yacht must account for this complexity and requires to set up suitable (experimental and numerical) tools able to describe as accurately as possible the system, in order to achieve an optimal configuration.

To give an idea of the complex interactions that should be taken into account in the design process, let us bound to a simple example. One way to reduce the viscous resistance on the hull, that is the force in the course direction given by frictional effects,

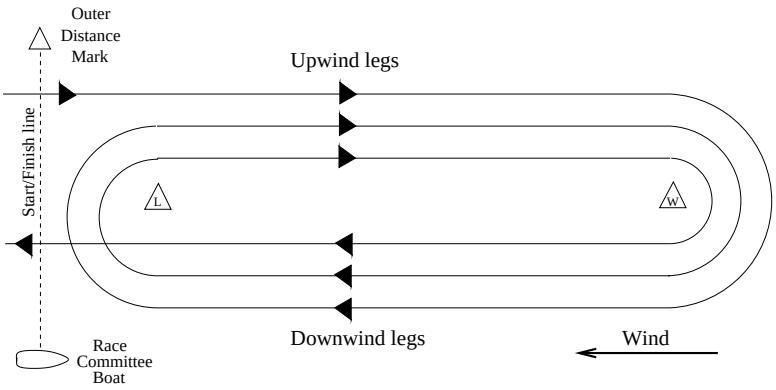

Figure 1: America's Cup race course.

is reducing its wetted surface. This can be accomplished by reducing its beam (width), keeping the same boat length. A reduction of beam decreases the heeling stability (*i.e.* the stability around the longitudinal centerline of the boat) and, consequently, the forces on the sails. We can see how a single change involves a domino effect on different areas of the design process.

In America's Cup match race, two buoys at a distance of 3.1 nautical miles are positioned in the wind direction. Three laps between the two buoys have to be completed, resulting in three upwind and three downwind legs (see Figure 1).

Upwind and downwind sailing call for different sailing techniques and the design of the boat should accommodate the conflicting requirements arising from the two regimes. For the sail rig, this problem is overcome through the use of different sets of sails (main and genoa for upwind sailing, main and spinnaker/gennaker for downwind sailing). On the other hand, in the underwater part, the possible changes during the race are restricted to the trimming of rudder and keel trim tab. Yacht appendices have to be designed to perform in both downwind sailing, where minimal drag should be attained, and in upwind sailing, where they have to resist the forces and moments generated by the sails.

Moreover, an America's cup yacht is constrained by the rules of the International America's Cup Class (IACC), which was first introduced in 1992 and since then it has continuously evolved from one edition to the next. For the 32^{nd} America's Cup edition that will take place in Valencia (Spain) during the summer 2007, a new edition (Version 5) of the IACC rules has been released. The major changes with respect to the previous version include a 1 tonne reduction of the boat displacement, deeper keels (+100 mm) and an increase in the maximum total sail area by around 50 m^2 downwind. These changes should make the racing closer with boats able to accelerate more readily and stand a better chance of closing the gap on the leading boat on the downwind leg.

The IACC rules impose severe restrictions on a number of design factors, not only on geometrical dimensions (depth, displacement, sail area), but also on flow control devices (*e.g.* number of underwater moving surfaces) and materials. The main rule that plays a crucial role in the evolution to the current America's Cup configuration is known as

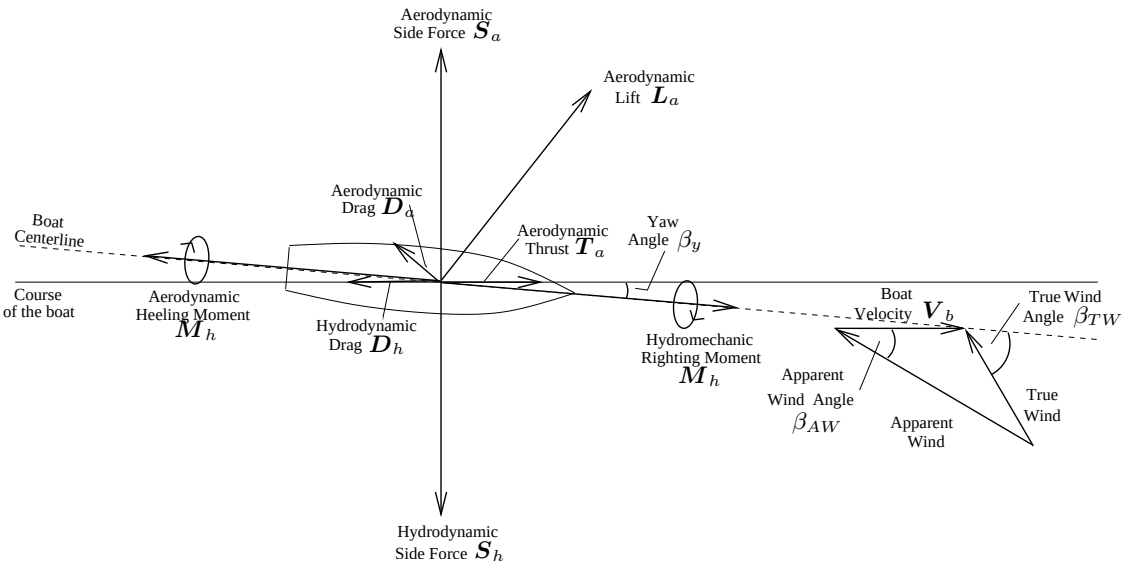

Figure 2: Forces and moments on the water plane.

"the Formula" and is in fact an inequality involving a relation between boat length L_b, sail area A_s and displacement D:

$$\frac{L_b + 1.25\sqrt{A_s} - 9.8\sqrt[3]{D}}{0.686} \leq 24 \text{ m} \tag{1}$$

A longer boat can be realized at the expense of lowering the sail area or increasing the displacement. Further unilateral constraints are dictated for boat length, beam, draft and displacement.

The standard approach adopted in the America's Cup design teams to evaluate whether a design change (and all the other design modifications that this change implies) is globally advantageous, is based on the use of a Velocity Prediction Program (VPP), which can be used to estimate the boat speed (and, in certain cases, the boat attitude) for any prescribed wind condition and sailing angle β_{TW} (the angle between the centerline of the boat and the wind direction). A numerical prediction of boat speed and attitude can be obtained by modeling the balance between the aerodynamic and hydrodynamic forces acting on the boat. A diagram representing the hydrodynamic and aerodynamic force as well as moment components acting in the water plane is presented in Fig. 2.

On the water plane, a steady sailing condition is obtained imposing two force balances in x direction (aligned with the boat velocity) and y direction (normal to x on the water plane) and a heeling moment balance around the centerline of the boat:

$$\begin{aligned} \boldsymbol{D}_h + \boldsymbol{T}_a &= 0, \\ \boldsymbol{S}_h + \boldsymbol{S}_a &= 0, \\ \boldsymbol{M}_h + \boldsymbol{M}_a &= 0, \end{aligned} \tag{2}$$

where $\boldsymbol{D}_h$ is the hydrodynamic drag (along the course direction), $\boldsymbol{T}_a$ is the aerodynamic thrust, $\boldsymbol{S}_h$ is the hydrodynamic side force perpendicular to the course, $\boldsymbol{S}_a$ is the aerodynamic side force, $\boldsymbol{M}_h$ and $\boldsymbol{M}_a$ are, respectively, the hydro mechanical righting moment and the aerodynamic heeling moment around the boat mean line. The angle β_Y between the course direction and the boat centerline is called *yaw* angle. The aerodynamic thrust and side force can be seen as a decomposition in the reference system aligned with the course direction of the aerodynamic lift and drag which are defined on a reference system aligned with the apparent wind direction (Fig. 2). Similar balance equations can be obtained for the other degrees of freedom.

In a VPP program, all the terms in system (2) are modeled as functions of boat speed, heel angle and yaw angle. Suitable correlation between the degrees of freedom of the system and the different force components can be obtained based on different sources of information: experimental results, theoretical predictions and numerical simulations. For a detailed presentation of Velocity Prediction Programs, we refer to [13, 5].

The role of advanced Computational Fluid Dynamics is to supply accurate estimates of the forces acting on the boat in different sailing conditions in order to improve the reliability of the prediction of the overall performance associated with a given design configuration. Since 1983, when the keel of Australia II was designed using computational methods [28], the subsequent America's Cup campaigns have always been characterized by an increasing interest in numerical simulations (see, e.g., [3, 4, 7, 6, 12, 20]).

In this paper, we describe the numerical methods adopted in the framework of the collaboration between the Ecole Polytechnique Fédérale de Lausanne (EPFL) and the Alinghi Team, in preparation to the 32$^{\text{nd}}$ edition of the America's Cup which will take place in Valencia (Spain) in summer 2007. A selection of the numerical results obtained on the different design aspects that have been investigated is also presented and discussed.

1 Mathematical Model

1.1 The flow equations

Let Ω denote the three-dimensional computational domain in which we solve the flow equations. If $\hat{\Omega}$ is a parallelepiped surrounding the boat B, the computational domain is the complementary of B w. r. to $\hat{\Omega}$, that is $\Omega = \hat{\Omega} \backslash B$ (see Fig. 3 for a two-dimensional sketch). The equations that govern the flow around B are the density-dependent (or inhomogeneous) incompressible Navier–Stokes equations, which read (see, e.g., [22]):

$$\frac{\partial \rho}{\partial t} + \boldsymbol{\nabla} \cdot (\rho \boldsymbol{u}) = 0 \tag{3}$$

$$\frac{\partial (\rho \boldsymbol{u})}{\partial t} + \boldsymbol{\nabla} \cdot (\rho \boldsymbol{u} \otimes \boldsymbol{u}) - \boldsymbol{\nabla} \cdot \boldsymbol{\tau}(\boldsymbol{u}, p) = \rho \boldsymbol{g} \tag{4}$$

$$\boldsymbol{\nabla} \cdot \boldsymbol{u} = 0 \tag{5}$$

for $\boldsymbol{x} \in \Omega$ and $0 < t < T$, and where ρ is the (variable) density, $\boldsymbol{u}$ is the velocity field, p is the pressure, $\boldsymbol{g} = (0, 0, g)^T$ is the gravity acceleration, and $\boldsymbol{\tau}(\boldsymbol{u}, p) = \mu(\boldsymbol{\nabla u} + \boldsymbol{\nabla u}^T) - p\boldsymbol{I}$ is the stress tensor with μ indicating the (variable) viscosity. The above equations have to be complemented with suitable initial conditions and boundary conditions. For the latter we typically consider a given velocity profile at the inflow boundary, with a flat farfield free-surface elevation.

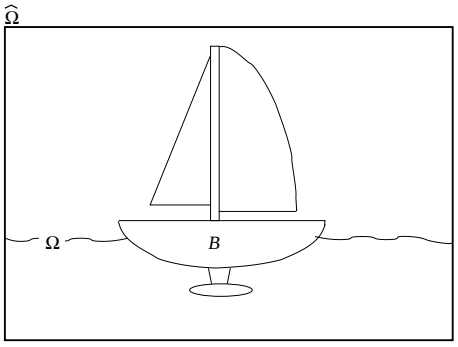

Figure 3: A two-dimensional section of the computational domain $\Omega = \hat{\Omega} \backslash B$

In the case we are interested in, the computational domain Ω is made of two regions, the volume Ω_w occupied by the water and that Ω_a occupied by the air. The interface Γ separating Ω_w from Ω_a is the (unknown) free-surface, which may be a disconnected two-dimensional manifold if wave breaking is accounted for. The unknown density ρ actually takes two constant states, ρ_w (in Ω_w) and ρ_a (in Ω_a). The values of ρ_w and ρ_a depend on the fluid temperatures, which are considered to be constant in the present model. The fluid viscosities μ_w (in Ω_w) and μ_a (in Ω_a) are constants which depend on ρ_w and ρ_a, respectively.

The set of equations (3)-(5) can therefore be seen as a model for the evolution of a two-phase flow consisting of two immiscible incompressible fluids with constant densities ρ_w and ρ_a and different viscosity coefficients μ_w and μ_a. In this respect, in view of the numerical simulation, we could regard equation (3) as the candidate for updating the (unknown) interface location Γ, then treat equations (4)-(5) as a coupled system of Navier–Stokes equations in the two sub-domains Ω_w and Ω_a:

$$\frac{\partial(\rho_w \boldsymbol{u}_w)}{\partial t} + \boldsymbol{\nabla} \cdot (\rho_w \boldsymbol{u}_w \otimes \boldsymbol{u}_w) - \boldsymbol{\nabla} \cdot \boldsymbol{\tau}_w(\boldsymbol{u}_w, p_w) = \rho_w \boldsymbol{g},$$

$$\boldsymbol{\nabla} \cdot \boldsymbol{u}_w = 0,$$

in $\Omega_w \times (0, T)$,

$$\frac{\partial(\rho_a \boldsymbol{u}_a)}{\partial t} + \boldsymbol{\nabla} \cdot (\rho_a \boldsymbol{u}_a \otimes \boldsymbol{u}_a) - \boldsymbol{\nabla} \cdot \boldsymbol{\tau}_a(\boldsymbol{u}_a, p_a) = \rho_a \boldsymbol{g},$$

$$\boldsymbol{\nabla} \cdot \boldsymbol{u}_a = 0,$$

in $\Omega_a \times (0,T)$. We have set $\boldsymbol{\tau}_w(\boldsymbol{u}_w, p_w) = \mu_w(\boldsymbol{\nabla}\boldsymbol{u}_w + \boldsymbol{\nabla}\boldsymbol{u}_w{}^T) - p_w\boldsymbol{I}$, while $\boldsymbol{\tau}_a(\boldsymbol{u}_a, p_a)$ is defined similarly.

The free surface Γ is a sharp interface between Ω_w and Ω_a, on which the normal components of the two velocities $\boldsymbol{u}_a \cdot \boldsymbol{n}$ and $\boldsymbol{u}_w \cdot \boldsymbol{n}$ should agree. Furthermore, the tangential components must match as well since the two flows are incompressible. Thus we have the following kinematic condition

$$\boldsymbol{u}_a = \boldsymbol{u}_w \quad \text{on } \Gamma. \tag{6}$$

Moreover, the forces acting on the fluid at the free-surface are in equilibrium. This is a dynamic condition and means that the normal forces on either side of Γ are of equal magnitude and opposed direction, while the tangential forces must agree in both magnitude and direction:

$$\boldsymbol{\tau}_a(\boldsymbol{u}_a, p_a) \cdot \boldsymbol{n} = \boldsymbol{\tau}_w(\boldsymbol{u}_w, p_w) \cdot \boldsymbol{n} + \kappa\sigma\boldsymbol{n} \quad \text{on } \Gamma, \tag{7}$$

where σ is the surface tension coefficient, that is a force per unit length of a free surface element acting tangential to the free-surface. It is a property of the liquid and depends on the temperature as well as on other factors. The quantity κ in (7) is the curvature of the free-surface, $\kappa = R_{t_1}^{-1} + R_{t_2}^{-1}$, where R_{t_1} and R_{t_2} are radii of curvature along the coordinates (t_1, t_2) of the plane tangentially to the free-surface (orthogonal to $\boldsymbol{n}$).

1.2 Modelling turbulence and transition

The flow around an IACC boat in standard race regime exhibits turbulent behaviour over the vast majority of the yacht surface. Turbulent flows are characterized by being highly unsteady, three-dimensional, containing vortices and coherent structures which stretch and increase the intensity of turbulence. Even more importantly, they fluctuate on a broad range of scales (in space and time). This feature makes the so-called direct numerical simulation (DNS) unaffordable. The adoption of a RANS (Reynolds Averaged Navier-Stokes) model is then required to deal with the turbulent nature of the flow.

The SST (Shear Stress Transport) model proposed by Menter [18] is an eddy-viscosity model defined as a combination of a $k-\omega$ model (in the inner boundary layer) and $k-\varepsilon$ model (in the outer region of and outside of the boundary layer). A blending function ensures a smooth transition between the two models.

The $k-\varepsilon$ model has two main weaknesses: it over-predicts the shear stress in adverse pressure gradient flows because of too large length scale (due to low dissipation) and it requires near-wall modification (i.e. low-Reynolds number damping terms). The $k-\omega$ model is better at predicting adverse pressure gradient flow and the standard model of Wilcox [29] does not use any damping functions. However, the disadvantage of the standard $k-\omega$ model is that it depends on the free-stream value of ω [17]. In order to improve both the $k-\varepsilon$ and the $k-\omega$ model, Menter [18] combines the two models. Prior to that, it is convenient to transform the $k-\varepsilon$ model into a $k-\omega$ model using the relation $\omega = \varepsilon/(c_\mu k)$.

The two partial differential equations governing the turbulent kinetic energy k and the turbulent frequency ω then reads:

$$\begin{aligned} \frac{D(\rho k)}{Dt} &= P_k - D_k + \boldsymbol{\nabla} \cdot ((\mu + \sigma_k \mu_t) \boldsymbol{\nabla} k) \\ \frac{D(\rho \omega)}{Dt} &= \alpha \rho \frac{P_k}{\mu_t} - D_\omega + Cd_\omega + \boldsymbol{\nabla} \cdot ((\mu + \sigma_k \mu_t) \boldsymbol{\nabla} \omega) \end{aligned} \tag{8}$$

where P_k and P_Ω are production terms, D_k and D_ω destruction ones and Cd_ω results from transforming the ε equation into an equation for ω. The coefficients in the SST model are obtained by combining the value of the coefficients of the standard $k - \omega$ (in the near wall region) to those of the $k - \varepsilon$ model by using a blending function F_1. We refer to [18] for a detailed description of the model and its parameters.

Eddy-viscosity turbulence models, such as the one described here, are nowadays widely adopted for the simulation of turbulent flows in engineering applications. Indeed, they are able to recover with an acceptable accuracy the global behaviour related to the turbulence nature of a flow. In particular, in presence of walls, they supply an accurate description of turbulent boundary layers.

The laminar-turbulent transition is physical phenomenon as complex as turbulence itself since involves the nonlinear interaction of flow perturbations that eventually evolves towards a fully turbulent behaviour. Many models for transition prediction have been proposed in the past decades [26, 15, 25, 16]. However, only recently transition models have been fully integrated into RANS solver. Among them, the Langtry-Menter transition model [19] is based on a transport equation for the turbulence intermittency γ which can be used to trigger transition locally. The intermittency function is coupled with the SST turbulence model introduced above by turning on the production term of the turbulent kinetic energy downstream of the transition point. In addition to the transport equation for the intermittency, a second transport equation is solved in terms of the transition onset momentum-thickness Reynolds number $\widetilde{\mathrm{Re}}_{\theta t}$. This is done in order to capture the non-local influence of the turbulence intensity, which changes due to the decay of the turbulence kinetic energy in the freestream, as well as due to changes in the free-stream velocity outside the boundary layer. This additional transport equation is an essential part of the model as it relates the empirical correlation to the onset criteria in the intermittency equation and allows the model to be used in general geometries without interaction from the user.

The intermittency equation is given by

$$\frac{D(\rho\gamma)}{Dt} = P_\gamma - E_\gamma + \boldsymbol{\nabla} \cdot \left(\left(\mu + \frac{\mu_t}{\sigma_f} \right) \boldsymbol{\nabla} \gamma \right) \tag{9}$$

where P_γ and E_γ are the production and destruction/relaminization terms, respectively. The production term P_γ is activated based on the value of the local vorticity Reynolds number. The onset criterion depends on the local value of the transition onset momentum-thickness Reynolds number $\widetilde{\mathrm{Re}}_{\theta t}$ which is computed by solving the following

transport equation

$$\frac{D(\rho\widetilde{\mathrm{Re}}_{\theta t})}{Dt} = P_{\theta t} + \boldsymbol{\nabla}\cdot\left(\sigma_{\theta t}(\mu+\mu_t)\boldsymbol{\nabla}\widetilde{\mathrm{Re}}_{\theta t}\right). \tag{10}$$

The source term $P_{\theta t}$ is defined as

$$P_{\theta t} = c_{\theta t}\frac{\rho}{t}\left(\mathrm{Re}_{\theta t} - \widetilde{\mathrm{Re}}_{\theta t}\right)(1-F_{\theta t})$$

where $\mathrm{Re}_{\theta t}$ is calculated from empirical correlation and $F_{\theta t}$ is a suitable blending function. Note that the empirical correlation is used only in the source term of the transport equation for transition onset momentum thickness Reynolds number (10).

The interplay between the transition model and the SST turbulence model leads to the following modifications in equations (8):

$$\begin{aligned}\frac{D(\rho k)}{Dt} &= \widetilde{P}_k - \widetilde{D}_k + \boldsymbol{\nabla}\cdot((\mu+\sigma_k\mu_t)\boldsymbol{\nabla}k) \\ \frac{D(\rho\omega)}{Dt} &= \alpha\rho\frac{P_k}{\mu_t} - \widetilde{D}_\omega + Cd_\omega + \boldsymbol{\nabla}\cdot((\mu+\sigma_k\mu_t)\boldsymbol{\nabla}\omega)\end{aligned} \tag{11}$$

with

$$\begin{aligned}\widetilde{P}_k &= \gamma P_k, \\ \widetilde{D}_k &= \min(\max(\gamma,0.1),1.0)D_k, \\ \widetilde{F}_1 &= \max\left(F_1, e^{-\left(\rho y\sqrt{k}/120\mu\right)^8}\right),\end{aligned}$$

and where P_k and D_k are the original production and destruction terms for the SST model and $\widetilde{F}_1$ replaces the original SST blending function F_1.

The CFD solver used in this work is Ansys-CFX. The RANS equations, as well as all the partial differential equations required in the turbulence, transition and free-surface models, are solved using a vertex-based finite volume method [24]. The free-surface is tracked using the Volume of Fluid (VOF) method [10].

1.3 Coupling with a 6-DOF rigid body dynamical system

The attitude of the boat advancing in calm water or wavy sea is strictly correlated with its performances. For this reason, a state-of-the-art numerical tool for yacht design predictions should be able to account for the boat motion. This requires the coupling between the fluid solver and a code able to compute the structure dynamics. In the case at hand, the structural deformations can be neglected and only the rigid body motion of the boat in the six degrees of freedom is considered.

Following the approach adopted in [1, 2], two orthogonal cartesian reference systems are considered: an inertial reference system (O, X, Y, Z) which moves forward with the mean boat speed and a body-fixed reference system (G, x, y, z), whose origin is the boat center of mass G, which translates and rotates with the boat. The XY plane

in the inertial reference system is parallel to the undisturbed water surface and the $Z - axis$ points upward. The body-fixed x-axis is directed from bow to stern, y is positive starboard and z upwards.

The dynamics of the boat in the 6 degrees of freedom is determined by integrating the equations of variation of linear and angular momentum in the inertial reference system, as follows

$$m\ddot{\boldsymbol{X}}_G = \boldsymbol{F} \tag{12}$$

$$\bar{\bar{\boldsymbol{T}}}\bar{\bar{\boldsymbol{I}}}\bar{\bar{\boldsymbol{T}}}^{-1}\dot{\boldsymbol{\Omega}} + \boldsymbol{\Omega} \times \bar{\bar{\boldsymbol{T}}}\bar{\bar{\boldsymbol{I}}}\bar{\bar{\boldsymbol{T}}}^{-1}\boldsymbol{\Omega} = \boldsymbol{M}_G \tag{13}$$

where m is the boat mass, $\ddot{\boldsymbol{X}}_G$ is the linear acceleration of the center of mass, $\boldsymbol{F}$ is the force acting on the boat, $\dot{\boldsymbol{\Omega}}$ and $\boldsymbol{\Omega}$ are the angular acceleration and velocity, respectively, $\boldsymbol{M}_G$ is the moment with respect to G acting on the boat, $\bar{\bar{\boldsymbol{I}}}$ is the tensor of inertia of the boat about the body-fixed reference system axes and $\bar{\bar{\boldsymbol{T}}}$ is the transformation matrix between the body-fixed and the inertial reference system ([1] for details).

The forces and moments acting on the boat are given by

$$\begin{aligned} \boldsymbol{F} &= \boldsymbol{F}_{\text{Flow}} + m\boldsymbol{g} + \boldsymbol{F}_{\text{Ext}} \\ \boldsymbol{M}_G &= \boldsymbol{M}_{\text{Flow}} + (\boldsymbol{X}_{\text{Ext}} - \boldsymbol{X}_G) \times \boldsymbol{F}_{\text{Ext}} \end{aligned}$$

where $\boldsymbol{F}_{\text{Flow}}$ and $\boldsymbol{M}_{\text{Flow}}$ are the force and moment, respectively, due to the interaction with the flow and $\boldsymbol{F}_{\text{Ext}}$ is an external forcing term (which may model, e.g., the wind force on sails) while $\boldsymbol{X}_{\text{Ext}}$ is its application point.

To integrate in time the equations of motion, the second order ordinary differential equations (12-13) are formulated as systems of first order ODE. If we consider, for example, the linear momentum equation (12), it can be rewritten as

$$m\dot{\boldsymbol{Y}}_G = \boldsymbol{F}, \tag{14}$$

$$\dot{\boldsymbol{X}}_G = \boldsymbol{Y}_G, \tag{15}$$

where $\boldsymbol{Y}_G$ denotes the linear velocity of the center of mass. This system is solved using an explicit 2-step Adam-Bashforth scheme for the velocity

$$\boldsymbol{Y}^{n+1} = \boldsymbol{Y}^n + \frac{\Delta t}{2m}(3\boldsymbol{F}^n - \boldsymbol{F}^{n-1}),$$

and a Crank-Nicholson scheme for the position of the center of mass

$$\boldsymbol{X}^{n+1} = \boldsymbol{X}^n + \frac{\Delta t}{2}(\boldsymbol{Y}^{n+1} + \boldsymbol{Y}^n).$$

For a convergence analysis of the scheme (as well as for a detailed description of the integration scheme for the angular momentum equation), we refer to [14], where it is shown that second-order accuracy in time is obtained. Moreover, the schemes features adequate stability properties. Indeed, the stability restriction on time step are less severe than the time step required to capture the physical time evolution.

In the coupling with the flow solver, the 6-DOF dynamical system receives at each time step the value of the forces and moments acting on the boat and returns values of new position as well as linear and angular velocity. In the flow solver, these data are used to update the computational grid (by a mesh motion strategy based on elastic analogy) and the flow equations are solved on the new domain through an Arbitrary Lagrangian Eulerian (ALE) approach.

2 Numerical Results

The numerical techniques described in the previous sections represent a relevant contribution for the improvement of the CFD technology adopted for IACC yacht design. In this section, we present an overview of the numerical results obtained on different design aspects during the preparation for the 2007 edition of the America's Cup, in collaboration with the Alinghi Team, defender of the Cup. In the same context, an advanced model for the simulation of the fluid-structure interaction between the flexible sails and the wind has been developed. The results of the research on this subject will be presented in a later paper [8].

2.1 Appendages optimization

One of the design areas where CFD simulations play a crucial role is the optimization of the appendages. Keel, bulb, winglets and rudder should be shaped and sized (within the degrees of freedom left by the strict IACC rules) in order to guarantee global optimal performances.

Full-scale tests are still an invaluable ingredient of the design process: the final step for taking every important design choice is always testing full scale on the real boat. Several days of testing, with the two boats differing by the design detail under investigation, are planned during every America's Cup campaign by all the syndicates.

Although the final choice between two keel designs is customary taken on the ground of two-boat testing comparisons and sailors' preference, the way the two final keel shapes are defined is determined by a deep numerical simulation analysis where many hundreds of different keel shapes are considered as candidates.

The design analyses that can be carried out by CFD simulations cover all the possible design variables that define a set of appendages. The great advantage of the numerical approach relies on the possibility to test several different configurations and to have a complete picture of the flow behaviour at every time instant.

Information about local distribution of flow quantities (such as, e.g. pressure, vorticity and turbulence intensity) can be very useful to improve the hydrodynamic performances. These information can be hardly obtained during a full-scale test and even in a fully equipped experimental facility (wind tunnel or towing tank) each of these data requires the setup of suitable measurement equipments. On the other hand, numerical simulations supply as outcome a complete database of relevant quantities about the considered flow problem.

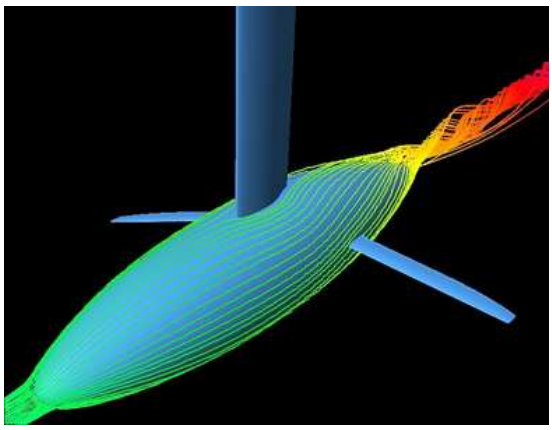

Figure 4: Streamlines around the appendages.

A complete reconstruction of the flow around the appendages can help understanding the formation of the main flow features (see, e.g., in Figure 4 a visualization of the vortex generated around the bulb) and their interaction with the boat components.

Another example of flow structure that can be captured by numerical simulations is the typical horseshoe vortex localized at the keel bulb intersection (see Figure 5, left). In this case, local change in the bulb shape (*dillets*) have been analysed in order to minimize the impact of this flow feature on the global performances. The range of boat speed and attitude in which the appendages can work efficiently (e.g., without leading to local flow separation or even stall) are also subject to numerical investigation. An accurate numerical model should be able to predict the occurrence of these kind of phenomena (see Figure 5, right).

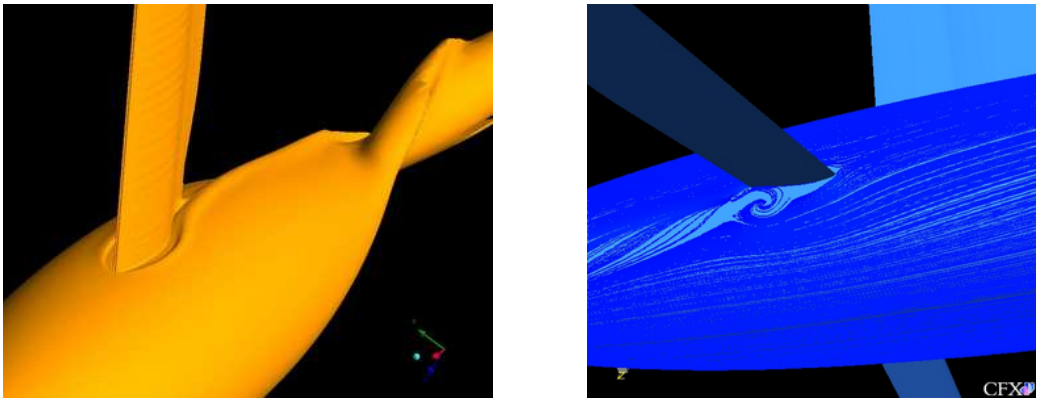

Figure 5: Isosurface of total pressure around bulb and keel displaying the horseshoe vortex generated around the keel-bulb junction (left) and separation bubble at the winglet-bulb junction (right).

The fluid-dynamic mechanism underlying the benefits observed when winglets are adopted is qualitatively displayed in Figure 6. Comparing appendage configurations with and without winglets shows that the latter have a strong impact on the vorticity evolution in the appendage wake. This effect is even stronger when increasing the yaw angle (and therefore the lift induced recirculation). Indeed, this vorticity reduction can be related to a reduction of the induced drag on keel and bulb, which is considered to be the most important beneficial effect induced by the presence of winglets.

The possibility to accurately predict the laminar-turbulent transition represents a big step forward in naval hydrodynamics, in particular for appendage design. Indeed, in this domain, the optimization process is often governed by trade-off analyses where pressure and viscous drag play one versus the other. A typical example is given by the comparison between a slender bulb and a shorter one (for constant weight/volume). If the former usually guarantees a lower pressure drag, this advantage is counteracted by a larger viscous drag due to the larger wetted surface. For this comparison, an accurate estimation of the transition location is required to predict the viscous component of the drag with an acceptable precision. Indeed, bulb and keel are often designed to work in

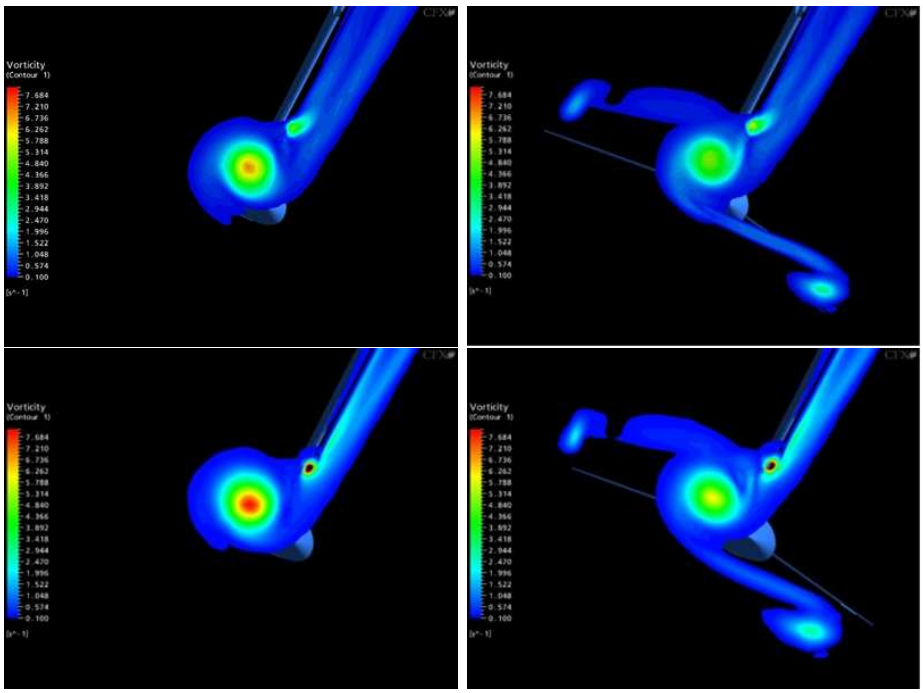

Figure 6: Cut plane of the vorticity field in the appendage wake. Top row: without (left) and with (right) winglets at 0 degree yaw angle. Bottom row: without (left) and with (right) winglets at 1.5 degree yaw angle.

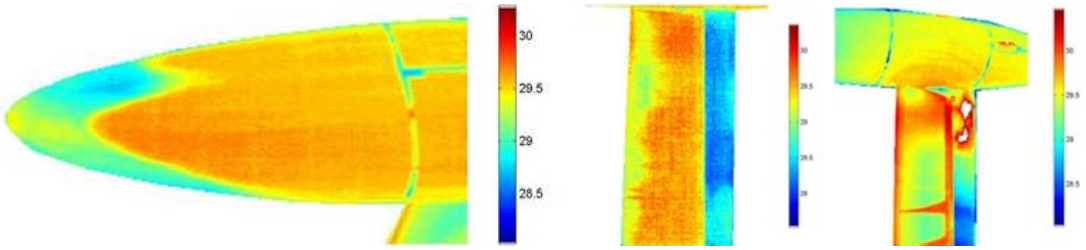

Figure 7: Results of the wind tunnel thermography: transition location on bulb (left), keel suction side (middle) and keel pressure side (right).

Component	Wind Tunnel	CFD
Bulb	7-15 %	8 %
Keel (Pressure side)	12-23%	24%
Keel (Suction side)	62 %	57%

Table 1: Comparison between experimental and numerical predictions for transition location.

a transitional regime where slight difference in shape can induce a significant change on the location where laminar-turbulent transition occurs.

As illustrated in Section 1.2, the transition model adopted is able to take into account not only natural transition mechanisms but also transition due to free-stream turbulence. In order to calibrate the model on the configuration we were interested in, experimental measurements have been carried on in the NCR's $9m \times 9m$ wind tunnel in Ottawa (Canada). A 1.5:1 model scale (larger than the full scale!) of the appendages was necessary in order to match the actual Reynolds number. A large amount of experimental data have been generated for the CFD calibration, including global and local (on each appendage element) force components, transition locations on keel and bulb, sensitivity analysis with respect to freestream turbulence intensity.

In Figure 7, the results of the wind tunnel thermography for an upwind configuration is presented. As expected, the extension of the laminarity region on pressure and suction side is very different. The laminar-turbulent transition is located based on the temperature gradient, since the heat exchange in a turbulent boundary layer is stronger than in a laminar one. The same upwind configuration has been simulated numerically. The laminar and turbulent regions on the appendage surface are displayed in Figure 8.

A quantitative comparison of laminarity extension on the different appendage elements is given in Table 1 and it seems to indicate that the model is able to predict with acceptable accuracy the transition location.

As mentioned above, the adoption of the transition model, giving an automatic way to estimate the transition location, is essential to compare different shapes with different

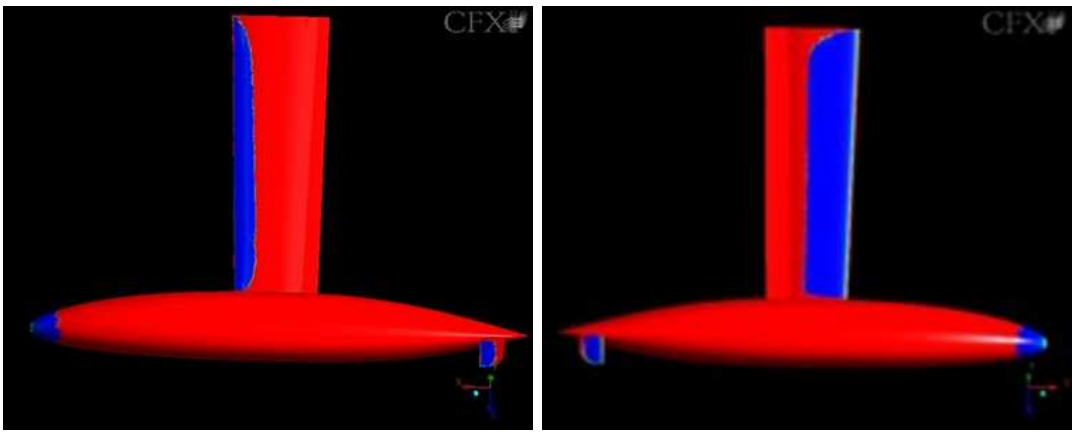

Figure 8: Results of the CFD transition analysis: transition location on suction side (left) and pressure side (right) of the appendages. Laminar regions are shown in red, turbulent ones in blue.

level of laminarity. A precise measure of the freestream turbulence intensity in wavy sea is often difficult to estimate. However, since a clear dependence of the transition location on the turbulence level imposed at the inlet boundary of the computational domain has been shown, the model can be calibrated based on the available experimental data. Indeed, when one experimental measure of the transition location on a reference configuration is known, it is possible to modify the inlet level of turbulence in order to match the transition location. In Table 2, the results of such kind of calibration are presented. In this case, a downwind symmetric appendage configuration is considered. Note that the value of inflow turbulent intensity that better matches the transition location measured in the wind tunnel is the same that guarantees the best correlation in terms of total force on the appendages. Laminar regions corresponding to different values of inflow turbulent intensity are shown in Figure 9.

Due to the grid requirements imposed by the transition and turbulence models, these simulations entail very large size computational grids (up to 20 millions elements). The simulations were run on the EPFL's Mizar cluster (450 AMD Opteron processors connected by a Myrinet network). The CPU time required for each simulation to reach convergence was about 30 hours on 32 processors.

TU	C_D	Error	Bulb Lam.	Keel Lam.
0.1%	0.0460	16%	18-26%	57%
0.15%	0.0483	12%	6-12%	57%
0.25%	0.0495	10%	5-6%	54%
0.5%	0.0558	1%	2-2.5%	29-36%
Exp.	0.0550		2%	27-30%

Table 2: Comparison between experimental and numerical predictions for transition location.

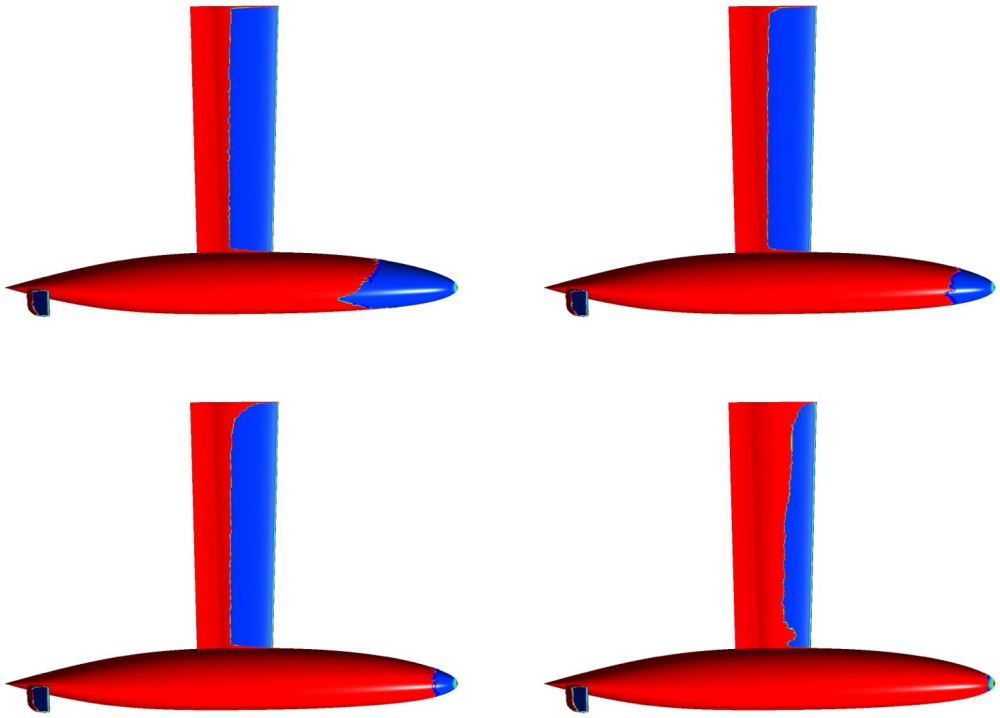

Figure 9: Transition locations for different values of freestream turbulence intensity. From top-left to bottom-right: $TU = 0.1, 0.15, 0.25, 0.5$.

2.2 Free-surface simulations

The wave drag can be quite significant fraction on an America's Cup hull, as much as the 60% of the total resistance at 10 knots of boat speed. An accurate determination of this component is important when comparing the performances of two hull designs. Local shape modifications require accurate analysis tools to correctly predict the performance differences deriving from these subtle changes.

In a typical hull design process, designers explore the performance of a family of hull shapes through a fast free-surface potential solver (see, e.g., [23]) to determine a set of candidates to be tested in the towing tank.

Numerical simulations based on RANS models are integrated into the design process in different ways: on one hand, they can be used to decrease the number of candidate shapes for which models are to be constructed and tested in the towing tank; moreover, they can be used to evaluate the free-surface flow in conditions where codes based on the panel method are unable to resolve critical differences due to viscous effects.

Hereafter, we present some numerical investigations carried out on the Series 60 benchmark hull with the model described in Section 1 where free-surface phenomena play a crucial role. Results on America's Cup hulls with comparisons with towing tank measurements are also presented and discussed.

2.2.1 Series 60 - Steady simulations

We first consider a standard free-surface test case for naval applications, that is the flow around the Series 60 $C_B = 0.6$ hull for which many experimental and numerical data are available (see, e.g., [27, 11, 1]). For the present study, the flow was computed at a Reynolds number Re=$4 \cdot 10^6$ and a Froude number Fr=0.316.

Different grid resolution are considered ranging from around 10000 elements for the coarsest grid to more than 1.5 millions for the finest. The wave pattern obtained on the finest grid is compared with the experimental data in Figure 10. The results in term of drag coefficients on the different grids are presented in Table 3 together with a comparison with the experimental data from [11]. The data and the waveline convergence on the hull given in Figure 11 indicate a good convergence of the numerical results to the experimental measurements.

Grid	$N_x \cdot N_y \cdot N_z$	C_t	C_p	C_f
1	$32 \cdot 12 \cdot 24$	0.0084	0.0053	0.0030
2	$64 \cdot 24 \cdot 48$	0.0064	0.0033	0.0031
3	$96 \cdot 32 \cdot 64$	0.0059	0.0026	0.0033
4	$192 \cdot 64 \cdot 128$	0.0056	0.0023	0.0033
Exp.	-	0.0058	-	-

Table 3: Drag coefficient convergence for the Series 60 test case, Fr=0.316.

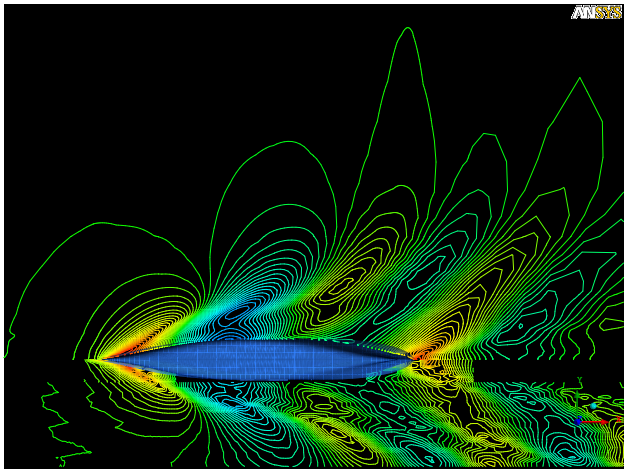

Figure 10: Wavepattern around Series 60 hull (Fr=0.316): numerical results on the finest grid (top) experimental data (bottom).

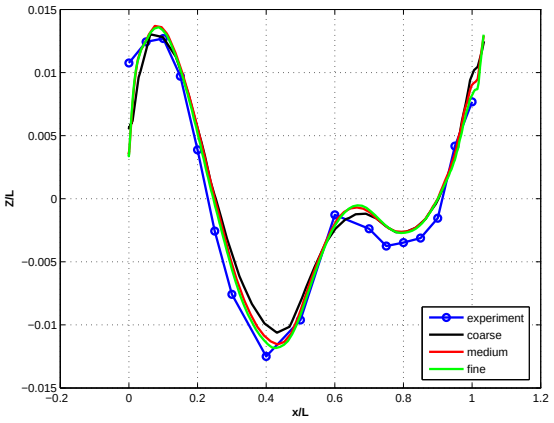

Figure 11: Wavelines on Series 60 hull for different grid resolution, Fr=0.316.

2.2.2 Series 60 - Dynamics in calm water

A complete set of validation studies on the coupling between the flow solver and the 6-DOF dynamical system has been carried out for the prediction of the ship's running attitude using the Series 60 hull. For a detailed description of the results we refer to [14].

We report one of these studies in which the stabilization behaviour of the hull subjected to a roll forcing moment (that may be due, for example, to a wind or current gust) has been analysed. We start from a steady symmetric solution and we impose a time dependent rolling moment given by

$$M_{x,\text{ext}} = 20H(0.5 - t)(\sin(2t))^2,$$

where H is the Heaviside function. Under this external moment the hull rotates by about 15 degrees and then, through a damped oscillation, stabilizes to the symmetric equilibrium state. The position of the hull and the free surface around it at different time instants during the stabilization process are reported in Figure 12.

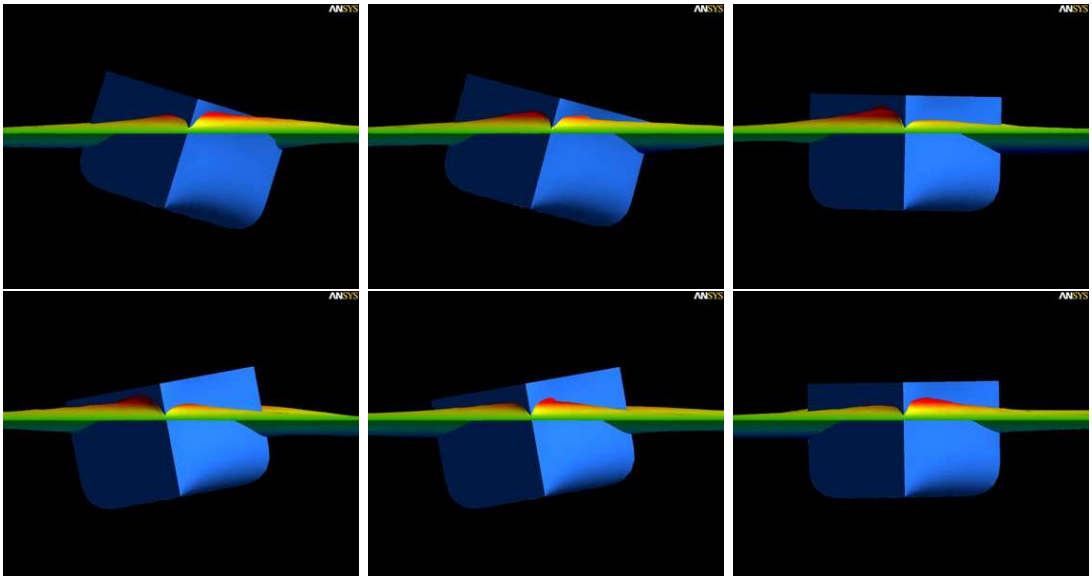

Figure 12: Bow wave around the hull at different time instant of the roll stabilization.

Two different roll moments of inertia, one double of the other, have been considered. The time evolution of the roll angle for the two cases is given in Figure 13. As expected, the hull with the smaller moment of inertia reaches a larger maximal roll angle and then undergoes a faster stabilization with a smaller oscillation period. In Table 4, we report the maximal amplitude of the oscillation $A_{\max}$, the period T and the damping factor defined as $\delta = \ln\left(\dfrac{\phi_j}{\phi_{j+1}}\right)$ where ϕ_j is the value of the roll angle at the j-th maximum.

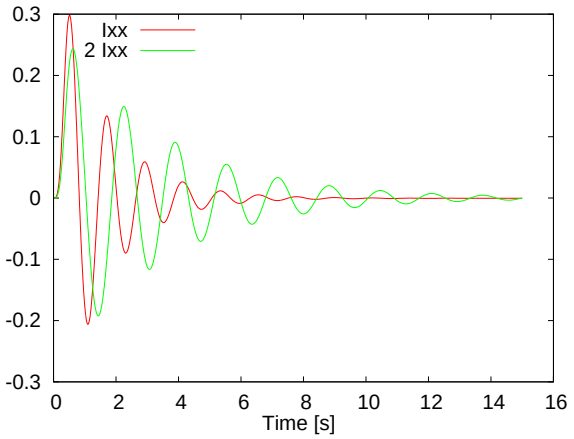

Figure 13: Time evolution of the roll angle with different moments of inertia.

This kind of analysis can be very useful to characterize the dynamic behaviour of a boat.

	$A_{\max}$	T	δ
I_{xx}	0.098L	1.21 s	0.8
$2I_{xx}$	0.080L	1.64 s	0.5

Table 4: Damped oscillation parameters for different moments of inertia

2.2.3 Series 60 - Dynamics in wavy sea

Although the simulations in calm water are already useful to understand some of the dynamical features of a hull and its natural frequencies with respect to each different degree of freedom, the potential benefits coming from the introduction of the boat motion model are fully exploited when the model is adopted for the analysis of the hull response in wavy sea.

To this purpose, an incoming wave model based on the fifth order Stokes wave expansion [9] has been implemented. This results in imposing a time dependent wave elevation and the correspondent orbital velocity at the inflow boundary of the domain.

We have considered a wave amplitude $\lambda = 0.05L$ where L is the boat length and different wave frequencies correspondent to incoming wave length of values in the range [0.5L,4L].

First a steady state simulation of the flow around the boat with no active degrees of freedom and without incoming wave (as described in Section 1) is performed and the solution is then used as initial condition for a time dependent simulation with incoming waves and the boat free to sink and trim. After a short transient the boat dynamics reaches an asymptotic periodic behaviour governed by the incoming wave characteristics.

The contours of the free-surface height at different time instants during one period is shown in Figure 14. We can appreciate the interaction between the incoming waves and the hull generated wave pattern.

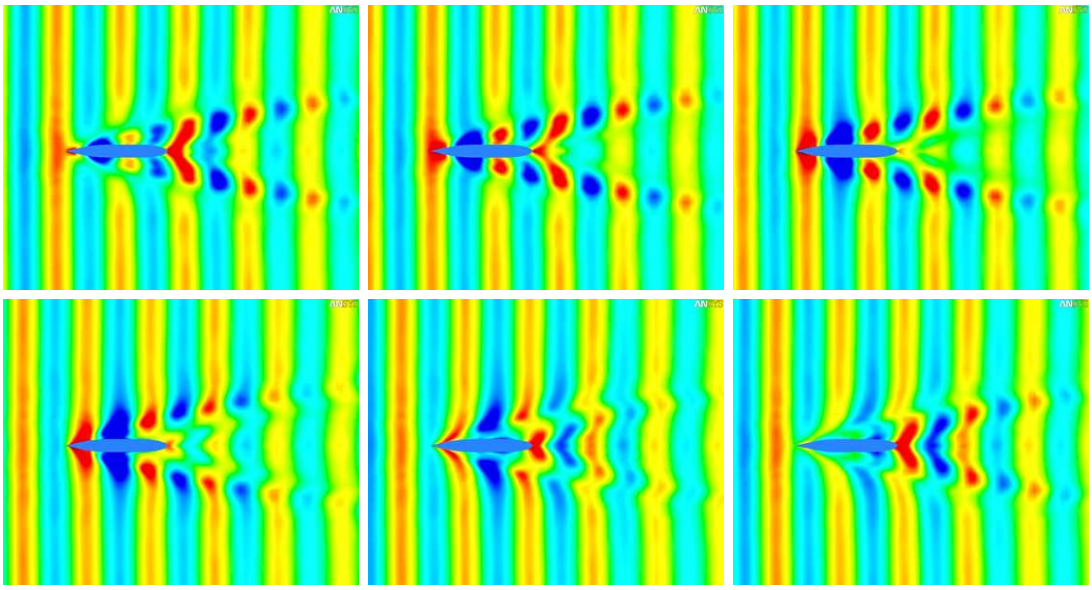

Figure 14: Contours of free-surface height at different time instant during one wave period.

The dynamical response of the boat to the periodic forcing generated by the incoming waves is presented in Figure 15 where the sink amplitude normalised to the incoming wave amplitude, $\xi = z/a$, is plotted against the incoming wave frequency ω. The figure clearly shows the presence of a resonance peak in correspondence to the natural sinking frequency of the boat. The time evolution of sink for different values of frequency is plotted in Figure 16 together with the corresponding wave profile. The amplitude of the sink oscillation is similar to the wave amplitude for low frequencies with the boat following the wave profile. The maximal amplitude is obtained with the natural sink frequency of the boat and is around the double than the wave amplitude. Finally, as expected, when encountering high frequency waves the sink response is almost null. For a detailed description of the implementation of the incoming waves into the flow solver and a complete presentation of the numerical results, we refer to [21].

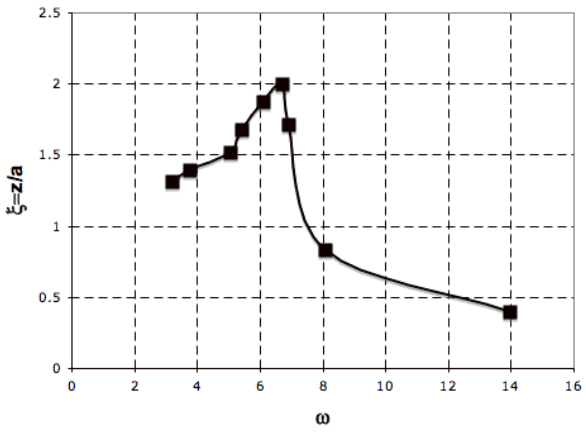

Figure 15: Dynamical response of the boat: sink amplitude as a function of the incoming wave frequency.

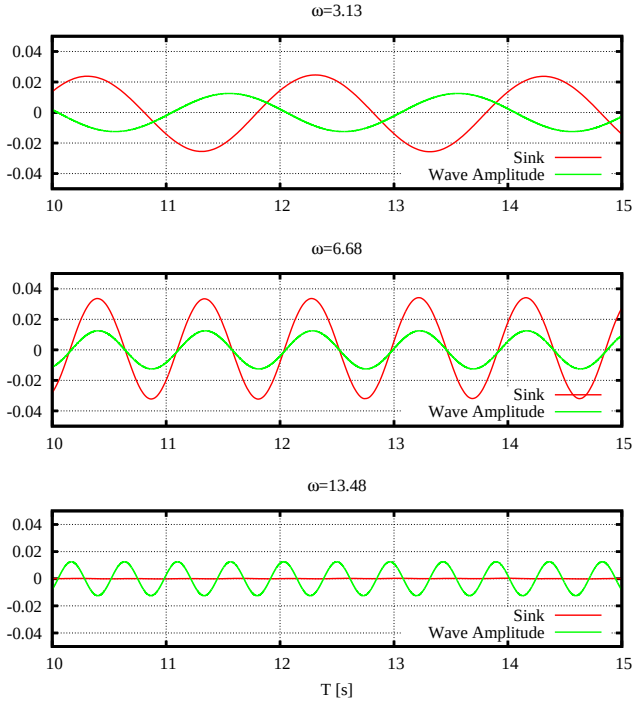

Figure 16: Asymptotic periodic behaviour of sink for different incoming wave frequency compared with the correspondent incoming wave amplitude.

2.2.4 IACC hull

The numerical scheme presented here for the prediction of boat dynamics can be a powerful tool in America's Cup yacht design. Many potential applications are being explored and range from the dynamic response in waves to manoeuvring. We expect this kind of numerical investigation could become the standard in the coming years.

Thus far, in the context of the America's Cup design, this approach has been used to reproduce towing tank experiments. Two IACC hull shapes, that will be referred to as Hull 1 and Hull 2, have been considered. The two hulls have different bow designs and towing tank experiments have been carried out to estimate drag and sink at different boat speeds.

Numerical simulations have been carried out with a similar setup as the one used for the Series 60 study, with just the sink degree of freedom activated, since in the towing tank the trim, as well as the other degrees of freedom, were fixed.

In Figure 17 we show the time history of the sink value starting from the initial sink position, correspondent to the hydrostatic equilibrium, and evolving through a damped oscillation towards the hydrodynamic equilibrium. The wave pattern around the two hulls at convergence are displayed in Figure 18.

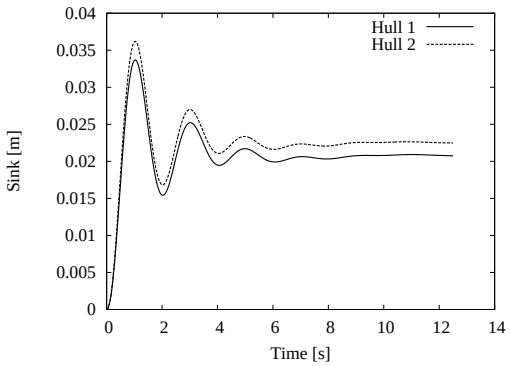

Figure 17: Time evolution of sink for the two hulls.

The numerical results show a good agreement in terms of forces and sink movement. A comparison between the total drag on Hull 1 obtained with the numerical simulations and the towing tank measurements at different boat speed is given in Figure 19, left. The error is consistently lower than 2% for all boat speeds. A similar comparison for the sink values at different boat speeds is presented in Figure 19, right. Again, we see a good correlation between numerical and experimental results.

In the yacht design context, a numerical tool able to accurately predict forces and attitudes is of utmost importance since it may reduce the need of carrying out expensive experimental sessions in towing tank facilities. In this respect, it is crucial for the numerical results to predict correct trends and variations between different configurations, even more than to give precise estimation of absolute values.

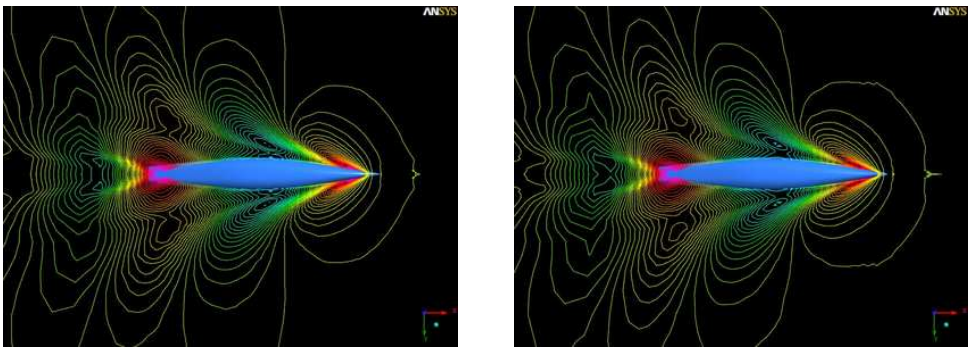

Figure 18: Wave patterns for Hull 1 (left) and Hull 2 (right) with a boat speed of 10 kts.

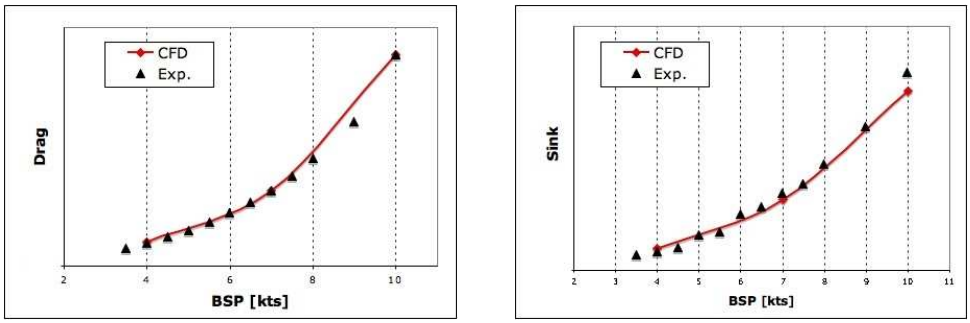

Figure 19: Drag (left) and sink (right) *vs.* boat speed: comparison between towing tank measurements and numerical predictions for Hull 1.

For the case at hand, a consistent rating between the two hull designs considered can be obtained from the numerical simulations as well as for the towing tank data, as shown in Table 5 where the drag deltas between Hull 2 and Hull 1 at different boat speeds are given.

BSP [kts]	(Hull 2-Hull 1) Drag Delta [N]	
	CFD	Exp.
4	0.62	0.32
7	0.79	0.41
10	4.15	2.87

Table 5: Comparison of the drag deltas between Hull 2 and Hull 1 obtained with towing tank measurements and numerical simulations.

Conclusions

In this work, we have presented some of the most recent results on numerical fluid-dynamic modelling obtained in the framework of the collaboration between the Ecole Polytechnique Fédérale de Lausanne and the Alinghi Team in preparation of the 32nd edition of the America's Cup.

We have highlighted the importance that CFD analysis is achieving in the design process of a racing yacht, devoting a particular attention to those modelling techniques that represent a step forward in this field.

Among them, we have presented and discussed through numerical examples the recent advances in transition modelling and its coupling with standard eddy-viscosity turbulence models. We have shown how accurate predictions on transition location can play a key role in the optimization of the appendages.

Finally, the coupling of a RANS solver with a 6-DOF dynamical model of the boat has been presented together with recent results of free-surface simulations of boat dynamics in calm and wavy water.

Acknowledgements

The authors wish to acknowledge the Alinghi Design Team for the support in explaining the complexity of America's Cup yacht design and Dr. Davide Detomi for his cooperation in this project. We also thank master students Matteo Lombardi and Simone Piazza for their contribution to the implementation of the 6-DOF dynamical system. This work has been funded by the Swiss Confederation's innovation promotion agency (KTI/CTI) through grant CTI-6972.1.

References

[1] R. Azcueta. *Computation of Turbulent Free-Surface Flows Around Ships and Floating Bodies*. Phd thesis, 2001.

[2] R. Azcueta. RANSE Simulations for Sailing Yachts Including Dynamic Sinkage & Trim and Unsteady Motions in Waves. In *High Performance Yacht Design Conference*, pages 13–20, Auckland, 2002.

[3] C. W. Boppe. Elements of Hull Optimization and Integration for Stars & Stripes. In *Proceedings of the Symposium on Hydrodynamic Performance Enhancement for Marine Applications*, 1988.

[4] M. Caponnetto, A. Castelli, R. Dupont, B. Bonjour, P.-L. Mathey, S. Sanche, and M. L. Sawley. Sailing Yacht Design Using Advanced Numerical Flow Techniques. In *Proceedings of the 14th Chesapeake Sailing Yacht Symposium*, Annapolis, USA, 1999.

[5] A. Claughton. Developments in the IMS VPP Formulations. In *Proceedings of the 14th Chesapeake Sailing Yacht Symposium*, Anapolis, USA, 1999.

[6] G. W. Cowles, N. Parolini, and M. L. Sawley. Numerical Simulation using RANS-based Tools for America's Cup design. In *Proceedings of the 16th Chesapeake Sailing Yacht Symposium*, Annapolis, USA, 2003.

[7] F. Jr. DeBord, J. Reichel, B. Rosen, and C. Fassardi. Design Optimization for the International America's Cup Class. In *Transactions of the 2002 SNAME Annual Meeting*, Boston, 2002.

[8] D. Detomi, N. Parolini, and A. Qaurteroni. Fluid-Structure Interaction Algorithms for Sailing Yacht Engineering. 2007. In preparation.

[9] J. D. Fenton. A Fifth-Order Stokes Theory for Steadywaves. *J. Waterway, Port, Coastal and Ocean Engineering*, 111:216–234, 1985.

[10] C. W. Hirt and B. D. Nichols. Volume of Fluid (VOF) Method for the Dynamics of Free Boundaries. *J. Comp. Phys.*, 39:201–225, 1981.

[11] C. E. Janson, K. J. Kim, and L. Larsson. Non-Linear Wave Pattern Calculations for the Series 60, CB=0.60 Hull. In *CFD Workshop*, Tokyo, 1994.

[12] P. Jones and R. Korpus. America's Cup class Yacht Design Using Viscous Flow CFD. In *Proceedings of the 16th Chesapeake Sailing Yacht Symposium*, Annapolis,USA, 2001.

[13] J. E. Kerwin. A Velocity Prediction Program for Ocean Racing Yachts. Technical Report 78-11, 1978. MIT Pratt Project Report.

[14] M. Lombardi. Simulazione Numerica della Dinamica di uno Scafo. Master thesis, Politecnico di Milano, 2006.

[15] R. E. Mayle. The Role of Laminar-Turbulent Transition in Gas Turbine Engines. *J. Turbomachinery*, 113:509–537, 1991.

[16] R. E. Mayle and A. Schulz. The Path to Predicting Bypass Transition. *J. Turbomachinery*, 119:405–411, 1997.

[17] F. R. Menter. Improved Two-Equation k-ω Turbulence Model for Aerodynamic Flows. Technical report, 1992. NASA TM-103975.

[18] F. R. Menter. Two-Equation Eddy-Viscosity Turbulence Models for Engineering Applications. *AIAA Journal*, 32(8):1598–1605, 1994.

[19] F. R. Menter, R. Langtry, S. Volker, and P. G. Huang. Transition Modelling for General Purpose CFD Codes. In *ERCOFTAC Int. Symp. Engineering Turbulence Modelling and Measurements*, 2005.

[20] N. Parolini and A. Quarteroni. Mathematical Models and Numerical Simulations for the America's Cup. *Comp. Meth. Appl. Mech. Eng.*, 173:1001–1026, 2005.

[21] S. Piazza. Simulazioni Numeriche della Dinamica di uno scafo in Mare Ondoso. Master thesis, Politecnico di Milano, 2007.

[22] A. Quarteroni and A. Valli. *Numerical Approximation of Partial Differential Equations*, volume 23 of *Springer Series in Computational Mathematics*. Springer-Verlag, Berlin, 1994.

[23] B. S. Rosen, J. P. Laiosa, W. H. Davis, and D. Stavetski. Splash Free-Surface Code Methodology for Hydrodynamic Design and Analysis of IACC Yachts. In *Proceedings of the 11th Chesapeake Sailing Yacht Symposium*, Anapolis, USA, 1993.

[24] G. E. Schneider and M. J. Raw. Control Volume Finite-Element Method for Heat Transfer and Fluidflow Using Colocated Variables. *Num. Heat Trans.*, 11:363–400, 1987.

[25] K. Sieger, R. Schiele, F. Kaufmann, S. Wittig, and W. Rodi. A Two-Layer Turbulence Model for the Calculation of Transitional Boundary-Layers. *ERCOFTAC bulletin*, 24:44–47, 1995.

[26] A. M. O. Smith and N. Gamberoni. Transition, Pressure Gradient and Stability Theory. Technical report, 1956. Douglas Aircraft Company, Long Beach, Calif. Rep. ES 26388.

[27] Y. Toda, F. Stern, and J. Longo. Mean-flow Measurement in the Boundary Layer and Wake and Wave Field of a Series 60 CB = 0.6 Ship Model. Part 1: Froude Numbers 0.16 and 0.36. *J. Ship Research*, 36(4):360–377, 1992.

[28] P. van Oossanen and P.N. Joubert. The Development of the Winged Keel for Twelve-Metre Yachts. *J. Fluid Mech.*, 173:55–71, 1986.

[29] D. C. Wilcox. Reassessment of the Scale-Determining Equation for Advanced Turbulence Models. *AIAA Journal*, 26:1299–1310, 1988.